

## Odd spin frustration in Cr(001) films thinner than three nanometers revealed by spin-polarized scanning tunneling microscopy

T. Kawagoe<sup>1</sup>,<sup>1</sup> R. Oka,<sup>1</sup> T. Miyamachi,<sup>2</sup> and S. Suga<sup>3</sup>

<sup>1</sup>*Division of Natural Science, Osaka Kyoiku University, Osaka 582-8582, Japan*

<sup>2</sup>*Department of Engineering Science, Graduate School of Informatics and Engineering, The University of Electro-Communications, 1-5-1, Chofu, Tokyo 182-8585, Japan*

<sup>3</sup>*The Institute of Scientific and Industrial Research, Osaka University, 8-1 Mihogaoka, Ibaraki, Osaka, 567-0047, Japan*



(Received 18 December 2020; revised 25 January 2021; accepted 8 February 2021; published 18 February 2021)

We have studied the surface structure and morphology of epitaxial Cr films on Au(001) substrate with Cr thickness ( $d_{\text{Cr}}$ ) below 3 nm. We have characterized the films prepared under various growth conditions by using scanning tunneling microscopy and spectroscopy (STM/STS), low-energy electron diffraction, and Auger electron spectroscopy. The good growth conditions of the Cr(001) films, which have atomically flat terraces without surface segregation of Au and with distinct surface states, are obtained by the following two methods. (I)  $d_{\text{Cr}} = 3$  nm film realized by two-step growth, i.e., first 1.5 nm of Cr deposited at room temperature ( $\sim 290$  K) and an additional 1.5 nm Cr deposition at 570 K and (II)  $d_{\text{Cr}} = 1.5$  nm film by room temperature growth and subsequently post-annealing at 470 K. The magnetic imaging of (I)  $d_{\text{Cr}} = 3$  nm Cr(001) film was performed by means of spin-polarized STM/STS. The observed magnetic image indicates that the topological antiferromagnetic (AF) order appears in a series of adjacent terraces and two types of spin frustration caused by screw dislocations lead to modifications of the topological AF order. One type of spin frustration is accompanied by narrow domain walls between two screw dislocations. The other type is a complex spin frustration caused by a cluster of an odd number of screw dislocations. The difference of the two types of spin frustration is explained through a micromagnetic simulation. We have also identified a large spin-frustrated area, consisting of a cluster of multiple number of screw dislocations.

DOI: [10.1103/PhysRevB.103.085427](https://doi.org/10.1103/PhysRevB.103.085427)

### I. INTRODUCTION

A variety of magnetic states in Cr films [1], such as a spin-density wave (SDW) and incommensurate antiferromagnetic (AF) ordering, have been of continuing interest since the discovery of the giant magnetoresistance in Fe/Cr multilayer films [2]. A reliable technique for imaging magnetic structures at the nanometer scale [3] is essential in the study of magnetism of Cr films. Spin-polarized scanning tunneling microscopy and spectroscopy (SP-STM/STS) [4] are suitable methods for such a purpose and are now established as techniques for magnetic imaging down to the atomic scale level [5]. Recently this technique was used to verify magnetic skyrmions [6,7] and Majorana fermions [8,9], which indicated that SP-STM/STS are important techniques to understand the physics of novel phenomena.

Experimental results of the magnetism of Cr films depend on several factors including the Cr thickness ( $d_{\text{Cr}}$ ) and adjacent layer materials contradicted from each other, particularly when  $d_{\text{Cr}} < 5$  nm [1]. A possible explanation is that the surface and interface on Cr films are not ideal, and the microscopic surface and interface structures including surface defects, roughness, and intermixing at the interface are playing crucial roles in the magnetism of these films. Then detailed information on topographic and magnetic structures is decisively important for the understanding of the magnetism of the Cr films. The SP-STM/STS technique has so far facili-

tated the successful separation of topographic, electronic, and magnetic information [4]. Therefore, further studies of the Cr thin film surface by SP-STM/STS studies are of deep interest.

A bulk Cr(001) surface exhibits “topological AF order” [10], in which Cr atoms within a single (001) plane has a ferromagnetic order, and the adjacent (001) plane shifted by a monatomic step height exhibited AF order with respect to the spin in the former plane. Using the SP-STS technique on the bulk Cr(001) surface at room temperature (RT), clear two-dimensional evidence of this topological AF order [11], and the impact of screw dislocation that leads to the spin frustration [12], were reported. SP-STS studies at temperatures in the range of 20–300 K revealed that the bulk Cr(001) surface maintains a topological AF order, which was attributed to the absence of the spin-flip in the region near the surface [13]. However, Hsu *et al.* reported the coexistence of the spin-density wave (SDW) and charge-density wave (CDW) on Cr(110) nanoislands on W(110) [14].

These experimental results indicate that a spin frustration occurs in the AF surface resulting from microscopic defects. A general understanding of the impact of structural defects on AF ordering may be important for the further development of spin-electronic devices as well as the fundamental physics of magnetism. The topological AF order of the Cr(001) surface is now well known as its magnetism is strongly correlated with the surface topography. Therefore, the Cr(001) surface can be used as a prototypical system to study spin frustration

caused by microscopic defects [11,12,15,16], which is also a particularly interesting topic for spin-polarized STM/STS studies. Few investigations focusing on the spin frustrations of the AF order, however, have been reported so far [11,12,15–19].

In a previous study we examined the surface magnetic structure of Cr(001) films at  $d_{\text{Cr}} = 4$  [15] and 9 nm [16] using SP-STM/STS. We identified topological AF order in a series of adjacent terraces, the existence of domains with different quantization axes, and narrow domain walls ( $\sim 6$  nm) near screw dislocations in 4-nm-thick Cr films [15]. In addition, we have successfully fabricated high-density nanoscale spiral terraces in 9-nm-thick Cr(001) films, where spin frustration and asymmetric magnetic ordering due to dense spiral terraces were observed [16]. SP-STM/STS studies of Cr(001) films on MgO(001) substrates with the contaminant-driven  $c(2 \times 2)$  surface structure were also reported [20,21]. The magnetic image of this system was observed consistent with the topological AF order.

The experimental results for Cr(110) nanoscale islands on W(110) [14] indicate that by reducing the dimensionality from bulk to ultrathin film, different types of magnetisms, such as the coexistence of topological AF order and SDW, and noncollinear magnetism is expected for epitaxial Cr(001) films being less than 3 nm thick. However, there are limited microscopic investigations on the surface and the interface structures, and magnetism of Cr(001) films with  $d_{\text{Cr}} \leq 3$  nm.

We report on the use of STM/STS, low-energy electron diffraction (LEED), and Auger electron spectroscopy (AES) for investigation of the growth of Cr(001) films prepared under various growth conditions. The SP-STS study of Cr(001) films ( $d_{\text{Cr}} = 3$  nm) is also presented. We have observed a novel type spin frustration: A complex spin frustration caused by a cluster of an odd number of screw dislocations and a large spin-frustrated area by a cluster of a multiple number of screw dislocations in contrast to the previous study of the spin frustration, which was the  $180^\circ$  type of domain wall between two screw dislocations [11,12,15].

## II. EXPERIMENTAL PROCEDURE AND PREPARATION OF CLEAN Au(001) SURFACE

The experiments were performed in an ultrahigh vacuum (UHV) system consisting of separate chambers for molecular-beam epitaxy (MBE) growth, STM, and sample load lock. The base pressure of the MBE and STM chambers were lower than  $5 \times 10^{-9}$  Pa. The MBE chamber is equipped with electron-beam evaporators for Cr and Fe, a Knudsen cell for Au, a resistive heating stage, and an apparatus for LEED and AES. The STM chamber is equipped with an STM unit, an electron bombardment unit for tip flash, and a sample transfer manipulator. The sample temperature was measured by a thermocouple mounted in close vicinity of the sample.

A clean Au(001) surface was prepared by the conventional MBE technique using an MgO(001) single-crystal substrate. The layer structure of the sample is schematically shown in Fig. 1(a). Before deposition, the MgO(001) substrate was annealed at 570 K for 4 h. As a buffer layer, the Fe(001) layer was grown at 290 K, with thickness of 2 nm. Au(001) film with a thickness of 100 nm was then epitaxially grown at

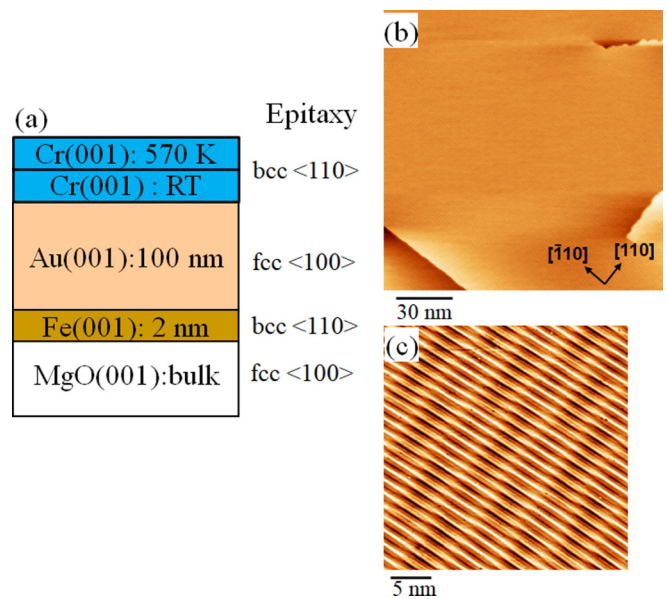


FIG. 1. (a) Typical layer structure of the sample employed in the experiment. Parallel aligned crystallographic axes in the surface plane depending on the epitaxial films are presented on the right side. (b) Large-scale ( $150 \times 150 \text{ nm}^2$ ) STM topographic image of a clean Au(001) surface after annealing at 570 K. Sample bias voltage ( $V_s$ ) and tunneling current ( $I_t$ ) were 0.3 V and 0.1 nA. Crystallographic direction of the fcc Au(001) surface is depicted in (b). (c) Higher resolution STM image ( $30 \times 30 \text{ nm}^2$ ,  $V_s = -1$  V,  $I_t = 0.1$  nA) of the clean Au(001) surface.

520 K on the Fe (001) buffer layer. After annealing at 570 K, the Au(001)-(5  $\times$  28) reconstructed surface [22] was confirmed by LEED and STM. A typical large-scale STM image of this Au(001) surface is presented in Fig. 1(b). Atomically flat terraces separated by a straight step and the presence of two screw dislocations are clearly identified on this Au(001) surface. The typical terrace width of the Au(001) surface is more than 100 nm. The height of the steps separating the neighboring terraces corresponds to the monatomic step height (0.202 nm). The step edges are aligned almost parallel to the Au(110) direction. A higher resolution STM image of the Au(001) surface is presented in Fig. 1(c). The atomically resolved STM image illustrates the (5  $\times$  28) reconstruction [23], which is characteristic of a clean Au(001) surface. We checked the quality of the Au(001) surface before every Cr deposition.

The Cr film was then grown on the clean and rather flat Au(001) surface at different growth temperatures with a growth rate of 0.14 nm/min. The pressure during the Cr evaporation was lower than  $1 \times 10^{-8}$  Pa. We prepared Cr films ( $d_{\text{Cr}} \leq 3$  nm) under different growth conditions. We characterized the structure and the cleanliness of the film by LEED and AES. STM measurements were then carried out at 290 K by an Omicron UHV micro-STM with a spring suspension and eddy-current dampers for vibration isolation. All topographic STM images were obtained in a constant-current mode using W tips or an Fe-coated W tip. The differential conductance ( $dI/dV$ ) was obtained by adding a 20 mV

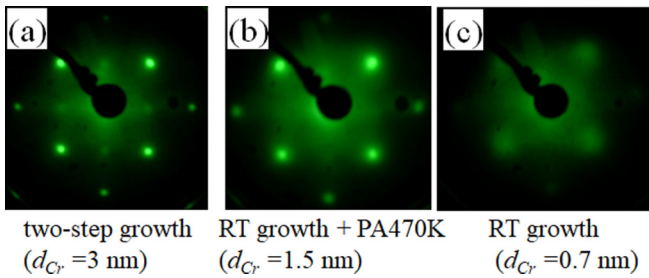


FIG. 2. (a)–(c) Typical LEED patterns of the Cr films obtained at 98.5 eV. (a)  $d_{Cr} = 3$  nm (prepared using the two-step growth method: RT growth of half and growth of the other half at 570 K). (b)  $d_{Cr} = 1.5$  nm (RT growth and subsequently PA at 470 K). (c)  $d_{Cr} = 0.7$  nm (RT growth only).

( $f = 3.33$  kHz) modulation to the DC gap voltage, and the  $dI/dV$  signal was detected using a lock-in amplifier.

### III. GROWTH OF Cr FILMS ON CLEAN Au(001) SURFACE

Suitable Cr(001) films for the SP-STM/STS study should have atomically flat and clean terraces with distinct surface states. Previously we prepared 4-nm-thick Cr(001) films using a two-step growth method [15]. In that case, the first 2 nm of the Cr was deposited on Au(001) at RT ( $\sim 290$  K) to avoid surface segregation of the Au. An additional 2 nm of Cr was deposited onto the already stacked Cr at a higher temperature of up to 570 K to improve the surface homogeneity. This procedure, which we call two-step growth in this paper, is similar to the growth of Fe(001) on Ag(001) [24].

We carefully prepared the Cr(001) films ( $d_{Cr} \leq 3$  nm) to minimize the surface roughness and surface impurity segregation. In this study we employed three different growth conditions: (1) the similar two-step growth method for  $d_{Cr} = 2$  and 3 nm, (2) RT growth and subsequently post-annealing (PA) at 470 or 570 K for  $d_{Cr} = 1.5$  nm, and (3) RT growth only for  $d_{Cr} = 0.7$  nm.

Figure 2 presents typical LEED patterns of the Cr films prepared under these different growth conditions: (a) the two-step growth ( $d_{Cr} = 3$  nm), (b) RT growth and PA at 470 K ( $d_{Cr} = 1.5$  nm), and (c) RT growth ( $d_{Cr} = 0.7$  nm). A fourfold  $p(1 \times 1)$  structure was observed in all LEED patterns. The observed fourfold  $p(1 \times 1)$  structure verifies that the Cr layers grow on the Au(001) surface with the epitaxial relationship of bcc Cr[110] // fcc Au[001]. Figures 2(a) and 2(b) are dominated by bright spots, which are characteristic of a clean Cr(001) surface, whereas diffused spots were observed for the RT growth film in Fig. 2(c). The observed strong LEED patterns in Figs. 2(a) and 2(b) are similar. However, significant differences in the sample preparations and thickness of Cr were clearly recognized on the characterizations by using STM, AES, and STS.

#### A. Cr films prepared using two-step growth method

We prepared the Cr(001) film with  $d_{Cr} = 3$  (2) nm shown in Figs. 3(a) and 3(b) by the two-step growth as follows: In the first step, 1.5 (1) nm of Cr was deposited at RT ( $\sim 290$  K), and further 1.5 (1) nm of Cr was deposited at 570 K.

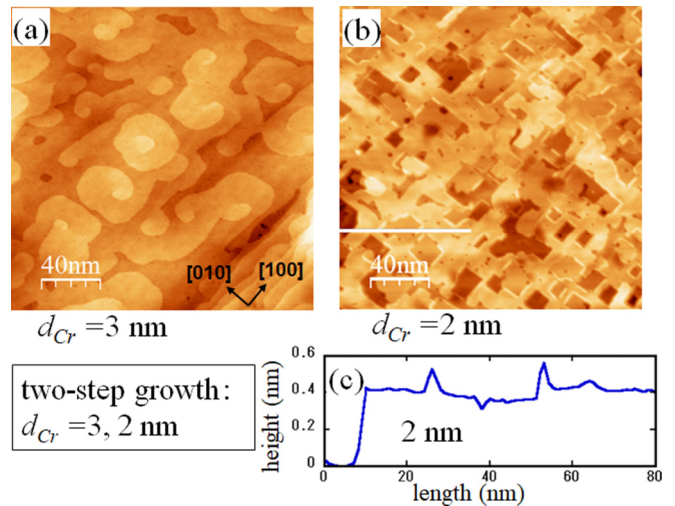


FIG. 3. (a) and (b) STM topographic images ( $200 \times 200$  nm<sup>2</sup>) of the Cr(001) films prepared by using the two-step growth method. (a)  $d_{Cr} = 3$  nm ( $V_s = 0.2$  V,  $I_t = 0.2$  nA) and (b)  $d_{Cr} = 2$  nm ( $V_s = 0.8$  V,  $I_t = 0.3$  nA). (c) Cross-sectional line profile along the horizontal white line in (b).

Figures 3(a) and 3(b) present the STM topographic images of these Cr(001) films. At  $d_{Cr} = 3$  nm, the film's surface is comprised mainly of an array of atomically flat terraces and round islands as recognized in Fig. 3(a). The typical lateral size of the terraces ranges from 20 to 50 nm and that of the islands ranges from 5 to 20 nm. The height of the steps that separated the adjacent terraces and islands corresponds always to the monoatomic layer height of Cr(001) (0.14 nm). These steps tend to be curved at corners but are preferentially aligned parallel to the Cr(100) direction. At the ends of most steps, screw dislocations are clearly visible.

In contrast, atomically flat terraces and several small rectangular holes are recognized at  $d_{Cr} = 2$  nm as shown in Fig. 3(b). The line profile along the white line in Fig. 3(b) is presented in Fig. 3(c). The depth of the rectangular hole is 0.40 nm, which corresponds to the two atomic layer height of Au(001). Slight sharp bumps are recognized at several places on this  $d_{Cr} = 2$  nm film. A similar inhomogeneous surface structure has been reported in our previous study on Co films on Au(001) after post-annealing at 500 K [25,26], in which a surface-segregated Au layer was identified.

To confirm the impact of the surface segregation of the Au for the film at  $d_{Cr} = 2$  nm, we compared the AES spectra obtained for both 3 and 2 nm films, which are presented in Fig. 4(a). At  $d_{Cr} = 3$  nm the AES spectrum is dominated by Cr LMM lines (445–570 eV). Although a small amount of C (<4%) signal (273 eV) can be recognized, the Au signals cannot be identified for  $d_{Cr} = 3$  nm. In the spectrum for the  $d_{Cr} = 2$  nm film, on the other hand, the Cr signals (445–570 eV) are substantially reduced (approximately down to 15% of that at  $d_{Cr} = 3$  nm). Instead, prominent Au signals (240 and 256 eV) can be recognized. The other elements such as O, S, and N are below the AES sensitivity limit of <1% in both spectra. We concluded that the Cr film for  $d_{Cr} = 3$  nm shown in Fig. 3(a) have atomically flat terraces without Au segregation, whereas an inhomogeneous surface

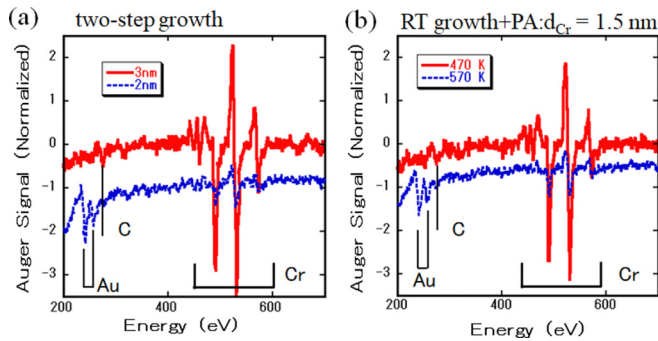


FIG. 4. Auger-electron spectra on the Cr(001) films. (a) Sample prepared by using the two-step growth method: RT growth of half and growth of the other half at 570 K ( $d_{\text{Cr}} = 3$  and 2 nm), and (b) prepared by RT growth and subsequently PA at 470 or 570 K ( $d_{\text{Cr}} = 1.5$  nm).

structure caused by the surface segregation of the Au was found on the film for  $d_{\text{Cr}} = 2$  nm in Fig. 3(b).

### B. Annealed Cr films at $d_{\text{Cr}} = 1.5$ nm

In the case of  $d_{\text{Cr}} \leq 2$  nm, it is thus found to be difficult to avoid the surface segregation of Au in Cr films even by the two-step growth method with the later half film grown at 570 K. Therefore, we have then prepared the Cr(001) films at  $d_{\text{Cr}} = 1.5$  nm by using RT ( $\sim 290$  K) growth and subsequently PA at 470 or 570 K and checked the surface quality. As shown in Fig. 4(b), the Auger spectra for  $d_{\text{Cr}} = 1.5$  nm Cr films annealed at 470 and 570 K have shown much different behavior. Namely, the Au segregation is much suppressed for the film annealed at 470 K.

Figures 5(a) and 5(b) present STM images of the Cr(001) films with  $d_{\text{Cr}} = 1.5$  nm annealed at (a) 570 K and (b) 470 K. The scan size is  $200 \times 200$  nm<sup>2</sup>, which is the same as that of the image presented in Fig. 3(a). In Fig. 5(a) (RT growth and PA at 570 K) we can identify atomically flat terraces, round-edged islands on them, and steps aligned parallel to the Cr  $\langle 100 \rangle$  directions, similar to those in Fig. 3(a). The typical lateral size of the terraces ranged from 5 to 40 nm, which is slightly smaller than that of Fig. 3(a). Several deep grooves elongated along the  $\langle 100 \rangle$  direction can be identified on the surface. These grooves represent the bunching steps on the Au(001) substrate.

Figure 5(b) presents an STM image of the film prepared by RT growth and PA at 470 K. The surface morphology differs significantly from that of the film shown in Fig. 5(a). Atomically flat terraces with widths greater than 10 nm are not at all observed. Instead, numerous small islands of different shapes and sizes can be identified. Figure 5(c) presents an enlarged STM image of the Cr films (PA at 470 K) at higher resolution (scan size:  $50 \times 50$  nm<sup>2</sup>). The surface morphology consists mainly of arrays of rather rectangular terraces with limited curving steps and the rectangular islands formed on them [Fig. 5(c)]. The line profile along the gray line in Fig. 5(c) is presented in Fig. 5(d). This line profile indicates that the film annealed at 470 K has atomically flat terraces (of width 5–10 nm) separated by 0.14 nm corresponding to the monatomic steps of the Cr(001) layer.

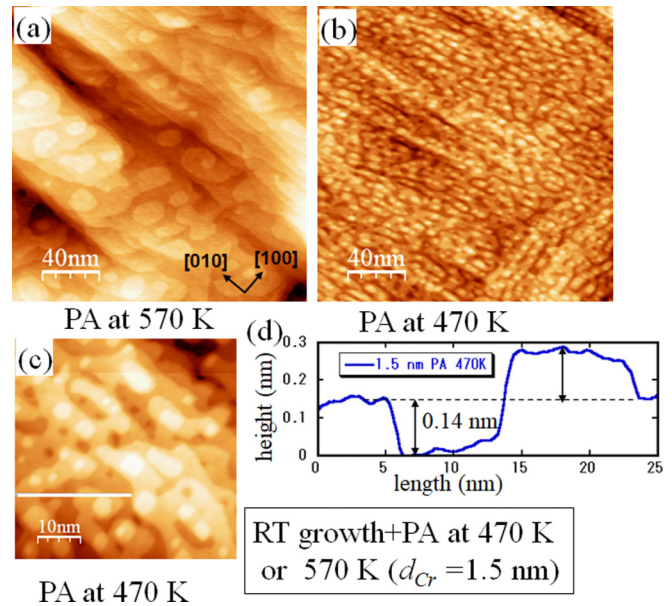


FIG. 5. STM images of the Cr(001) films ( $d_{\text{Cr}} = 1.5$  nm) prepared by RT growth and PA at 570 or 470 K. The scan size is (a) and (b)  $200 \times 200$  nm<sup>2</sup>, and (c)  $50 \times 50$  nm<sup>2</sup>. (a) PA at 570 K ( $V_s = -0.2$  V,  $I_t = 0.2$  nA), (b) and (c) PA at 470 K [(b)  $V_s = 0.5$  V,  $I_t = 0.2$  nA and (c)  $V_s = 0.2$  V,  $I_t = 0.5$  nA]. (d) Cross-sectional line profile along the horizontal white line in (c). 0.14 nm is the monolayer height of Cr(001).

### C. RT growth film with $d_{\text{Cr}} = 0.7$ nm

As-grown Cr film with  $d_{\text{Cr}} = 0.7$  nm is also compared with thicker Cr films prepared by (1) the two-step growth method and (2) RT growth and subsequently PA at 470 or 570 K. A large-scale ( $200 \times 200$  nm<sup>2</sup>) STM image of the just as-grown  $d_{\text{Cr}} = 0.7$  nm Cr film at RT ( $\sim 290$  K) is shown in Fig. 6(a). The film's surface is comprised mainly of numerous small islands with different shapes and sizes. These islands are a little

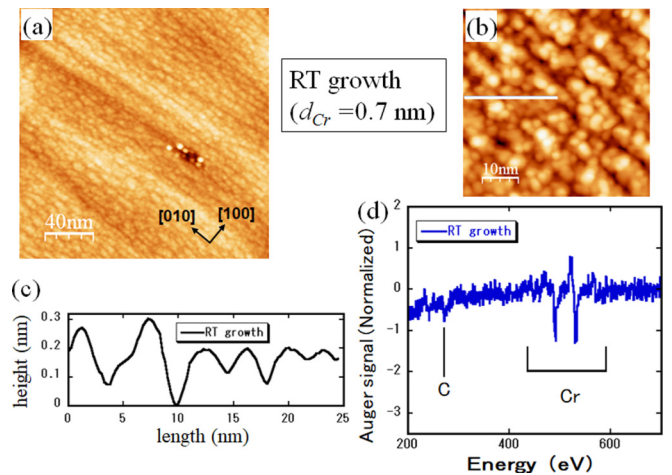


FIG. 6. STM images of the Cr(001) films ( $d_{\text{Cr}} = 0.7$  nm) prepared by RT growth. The scan size is (a)  $200 \times 200$  nm<sup>2</sup> and (b)  $50 \times 50$  nm<sup>2</sup>. (c) Cross-sectional line profile along the horizontal white line in (b). (d) Auger-electron spectrum on the Cr(001) film prepared by RT growth.

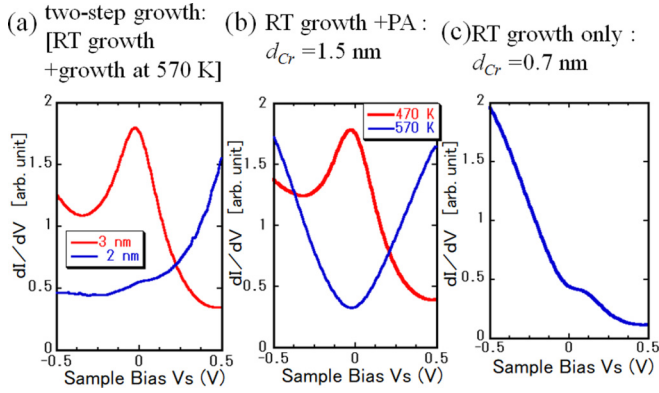


FIG. 7. Averaged tunneling  $dI/dV$  spectra of the Cr(001) film surfaces. (a) Sample prepared by using the two-step growth method: RT growth of half and growth of the other half at 570 K. ( $d_{Cr} = 3$  and 2 nm), (b) prepared by RT growth and subsequently PA at 470 or 570 K ( $d_{Cr} = 1.5$  nm), and (c) prepared by RT growth ( $d_{Cr} = 0.7$  nm).

bit elongated along the  $\langle 100 \rangle$  direction of the Cr(001) surface, where the typical island length is evaluated around 20 nm in Fig. 6(a). A higher resolution STM image ( $50 \times 50$  nm<sup>2</sup>) of the RT growth Cr film is presented in Fig. 6(b). Small round islands with a mean spacing of 5 nm are mostly observed. The line profile along the white line in Fig. 6(b) is presented in Fig. 6(c), which indicates that the film grown at RT ( $\sim 290$  K) is not comprised of atomically flat terraces, as expected from the diffused LEED pattern shown in Fig. 2(c). The AES spectrum of the RT growth is also shown in Fig. 6(d). The intensity of the Cr signals (445–570 eV) is reduced 42% of that of Fig. 4(b) (the  $d_{Cr} = 1.5$  nm film PA at 470 K), due to the decrease in  $d_{Cr}$  down to 0.7 nm. However, the Cr signals is dominated and the Au signals cannot be identified for RT growth film at  $d_{Cr} = 0.7$  nm.

#### D. Tunneling spectra on Cr(001) film surfaces

Figures 7(a)–7(c) present averaged  $dI/dV$  spectra of the Cr(001) film prepared by three different growth conditions: (a) the two-step growth, (b) RT growth and PA at 470 or 570 K, and (c) RT growth. A distinct peak in Fig. 7(a) near the Fermi level ( $V_s = -30$  mV) is observed for the  $d_{Cr} = 3$  nm film prepared by the two-step growth. A very similar peak feature is observed in Fig. 7(b) for the film prepared by RT growth and PA at 470 K ( $d_{Cr} = 1.5$  nm), as previously reported by Strosio *et al.* [27]. This peak is identified as the  $d_{z^2}$ -like highly spin-polarized (minority-spin) surface state. The AES spectra of both films (two-step grown  $d_{Cr} = 3$  nm film and RT grown and PA at 470 K  $d_{Cr} = 1.5$  nm film) shown in Fig. 4 confirm the successful suppression of the surface segregation of Au.

In contrast, the observed  $dI/dV$  spectra for the two step grown  $d_{Cr} = 2$  nm film in Fig. 7(a) and the  $d_{Cr} = 1.5$  nm film PA at 570 K in Fig. 7(b) [presented by blue curves in Fig. 7(a) and 7(b)], in which Au segregation was observed, have shown no distinct peaks. The  $dI/dV$  spectrum for RT growth film with  $d_{Cr} = 0.7$  nm [Fig. 7(c)] exhibits only a weak peak sign (not a distinct peak) at  $V_s = +50$  mV, whereas the AES

spectrum of the film grown at RT indicates the successful suppression of the surface segregation of Au. It is reported that the scattering of the spin-polarized electrons by grain boundaries could account for the absence of the spin-polarized surface states [28]. Then the magnetic imaging to check the surface segregation and atomic flatness of the prepared Cr surfaces is thought to be a prerequisite for the SP-STM/ STS studies.

The experimental results of the LEED, AES, STM, and STS techniques used to qualify the Cr growth are summarized in Table I. The Cr(001) films that are suitable for the SP-STM/STS study should have atomically flat terraces without surface segregation of Au and have distinct spin polarization resulting from the surface states. Table I of the experimental results indicates that these requirements are satisfied under the condition of  $d_{Cr} = 3$  nm: Two-step growth methods.

#### IV. MAGNETIC IMAGING OF Cr(001) FILMS PREPARED UNDER OPTIMIZED GROWTH CONDITIONS

In the SP-STM/STS experiment we used an Fe-coated W tip, which was sensitive to the in-plane magnetic moments. After an etched W tip was cleaned *in situ* by a flash at high temperatures ( $T > 2200$  K), 2-nm-thick Fe was deposited on it at 290 K and subsequently annealed at 420 K for 1 min. The  $dI/dV$  signal intensity, or magnetic contrast, for the spin-dependent tunneling can be described as [4]

$$dI/dV \propto (1 + P_t P_s \cos \theta), \quad (1)$$

where  $P_t$  and  $P_s$  are the spin polarization of the tip and the sample, respectively.  $\theta$  is the relative angle of the magnetization between the tip and the sample. Since the tip magnetization is fixed, and  $P_s$  is considered to be constant in our experiment, the  $dI/dV$  intensity maps reflect the local orientation of the sample surface magnetization with respect to the tip magnetization [4,15]. Based on the spin-polarized tunneling using the Fe coated W tip, we performed imaging of the magnetic structure on the Cr(001) film surface. A sample bias voltage  $V_s$  was tuned to be near the Cr(001) surface state peak for this purpose. Here we present the results for the  $d_{Cr} = 3$  nm Cr(001) films prepared by the two-step growth method.

##### A. SP-STs study of two-step growth Cr(001) films with $d_{Cr} = 3$ nm

A topography image and a corresponding  $dI/dV$  map (magnetic image) at  $V_s = -200$  mV (tail part of the before mentioned peak) are simultaneously acquired for the same area as shown in Figs. 8(a) and 8(b), respectively. In the topographic STM image [Fig. 8(a)], an array of relatively large terraces (50–100 nm) and islands are recognized on the surface. Several curved steps are recognized, and both sides of the curve are preferentially aligned parallel to the Cr  $\langle 100 \rangle$  direction. Then the height profile along the white line in Fig. 8(a) is shown in Fig. 8(c). The height of the steps that separate the neighboring terraces and islands corresponds always to the Cr monatomic layer height (0.144 nm). Several steps form a spiral trajectory. At the central ends of these steps, the screw dislocations can be identified. These topographic

TABLE I. Summary of experimental results of LEED, AES, STM, and STS techniques used to investigate the growth and surface quality of the Cr(001) films. Post annealing (PA) was performed at either 570 or 470 K for the 1.5 nm film.  $d_{\text{Cr}}$  is the Cr thickness.

$d_{\text{Cr}}$ (nm)	Sample preparation	LEED pattern (Fig. 2)	Suppression of Au segregation (AES)	Flatness (terrace width) (STM)	SP-surface state (STS) (Fig. 7)
3	Two-step growth: (1.5 nm RT + 1.5 nm at 570 K)	$p(1 \times 1)$ bright	○ Yes	○ 20–50 nm	○ distinct peak
2	Two-step growth: (1 nm RT + 1 nm at 570 K)	$p(1 \times 1)$ bright	× No	× inhomogeneous	× no peak
1.5	RT + PA 570 K	$p(1 \times 1)$ diffused	× No	△ 10–40 nm	× no peak
1.5	RT + PA 470 K	$p(1 \times 1)$ bright	○ Yes	△ 5–10 nm	○ distinct peak
0.7	RT only	$p(1 \times 1)$ diffused	○ Yes	× islands	× no peak

features are almost equivalent to those shown in Fig. 3(a). We identified six screw dislocations in the scanned area of Fig. 8.

In the  $dI/dV$  map [Fig. 8(b)], the locations of the steps and screw dislocations are represented by the white lines and the orange dots, respectively. We observed distinct magnetic contrasts in Fig. 8(b). By careful comparison of the two images

of Figs. 8(a) and 8(b), the  $dI/dV$  magnetic contrast in most of the areas alternates between two levels [blue and yellow colors in Fig. 8(b)] whenever the monatomic height difference of the terraces or islands is recognized. This is consistent with the topological AF order, which was observed in the bulk Cr(001) surfaces [11,12] as well as in our previous work on

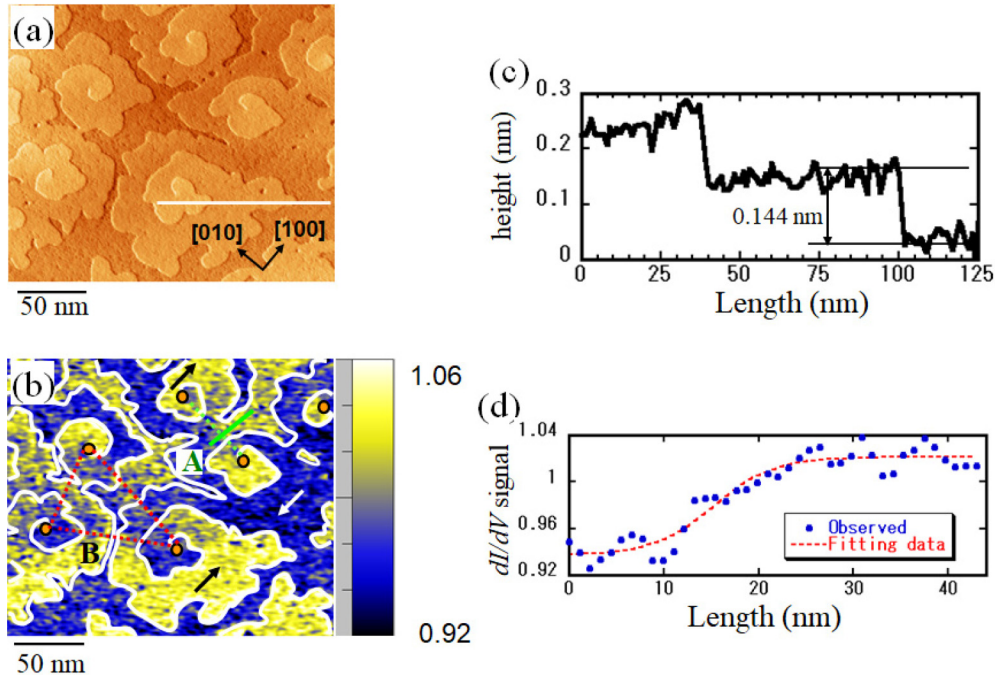


FIG. 8. STM images ( $235 \times 200 \text{ nm}^2$ ) of (a) the topography and (b)  $dI/dV$  map obtained simultaneously from the same area of two-step grown Cr(001) film surface ( $d_{\text{Cr}} = 3 \text{ nm}$ ) with the use of Fe coated W tip ( $V_s = -0.2 \text{ V}$ ,  $I_t = 0.2 \text{ nA}$ ). Crystallographic direction of the bcc Cr(001) surface is shown in (a). Steps and screw dislocations are indicated in (b) for clarity purpose by the white lines and orange dots, respectively. Magnetization directions in the individual region are shown by the black and white arrows (representing opposite directions). The representative AF domain wall A and the noticeable spin-frustrated area B [designated B in Fig. 8(b)] are indicated by green- and red-dotted triangular lines, respectively. (c) Cross-sectional line profile of height along the horizontal white line in (a). 0.144 nm is the monolayer height of Cr(001). (d) Cross-sectional line profile of the magnetic  $dI/dV$  signal along the full green line in the region A in Fig. 8(b). Red dashed curve shows a fit by Eq. (3)

4-nm-thick Cr(001) films [15]. A possible magnetic structure of the Cr(001) film surface is schematically indicated by the black and white arrows, assuming that the magnetic direction is parallel or antiparallel to the [100] direction.

We have also noticed that this topological AF order on the Cr(001) film was modified by the presence of the screw dislocations. We have observed two types of modifications of the topological AF order: (A) the spin modification bounded by two screw dislocations [at the end of green dotted line in Fig. 8(b)] and (B) the spin modification bounded by three screw dislocations located on the vertices of a triangle (defined by the red dashed lines). We call these type A and type B spin modifications in this paper. While both are resulting from the spin frustrations caused by screw dislocations, there is a clear difference between the two types of spin frustration.

The feature of type A spin frustration between the two screw dislocations is a  $180^\circ$  type domain wall between the two dislocations (represented by the green dotted line). On the other hand, feature B shows that the magnetic contrast vanishes noticeably within the triangular area (represented by red broken lines). It should be noted that the type B spin frustration consists of three screw dislocations and was neither observed on the bulk Cr(001) surface [11,12] nor in our previous study on 4-nm-thick Cr(001) films [15], whereas the type A spin frustration was already reported in bulk Cr(001) surfaces [11,12].

The feature of the type A spin frustration between two screw dislocations can be understood by the following reasons: (1) the  $180^\circ$  type of domain wall is due to the uniaxial anisotropy, (2) the domain wall starts from one screw dislocation and is annihilated into another screw dislocation due to the cancellation of spin frustration, and (3) the domain wall connects between two screw dislocations with a straight line because the total energy is minimized by the shorter length of the walls.

Ravlić *et al.* reported that a width of the  $180^\circ$  type of domain walls in the bulk Cr(001) surface was approximately 120–170 nm [12]. The intrinsic domain wall width  $w$  is usually determined by [12]

$$w = 2\sqrt{A_{\text{ex}}/K_u} = 2\lambda, \quad (2)$$

where  $A_{\text{ex}}$  is the exchange stiffness,  $K_u$  is the effective uniaxial anisotropy energy density, and  $\lambda$  corresponds to the exchange length. In the case of the bulk Cr(001) surface, the  $180^\circ$  type of domain walls were created and annihilated at every screw dislocation connected with a straight line, realizing the intrinsic domain wall width. Therefore, the observed domain wall width (approximately 150 nm) on the bulk Cr(001) surface may be considered as the intrinsic domain wall width ( $2\lambda$ ) of the Cr(001) surface. They also studied the dependence of the domain-wall width on the distance from the screw dislocation experimentally and compared it with the results of micromagnetic simulations. At smaller distances from the screw dislocation ( $<60$  nm), narrower domain walls (15–100 nm) were found on bulk Cr(001) surface [12].

We also reported the type A spin frustration between two screw dislocations on 4-nm-thick Cr(001) films [15]. The observed width of the domain wall was significantly smaller ( $\sim 6$  nm) relative to that observed on the bulk Cr(001) surface.

This difference is attributed to the shorter distance between the two screw dislocations in the thin Cr(001) films due to the high-density dislocations [15] compared to the intrinsic domain wall width (approximately 150 nm) on the bulk Cr(001) surface.

In Fig. 8(b) we also observed AF domain wall on straight lines between two dislocations, which are represented by the green dotted line in region A. The line profile of the magnetic  $dI/dV$  signal along the full green line in region A across the domain wall in Fig. 8(b) is shown in Fig. 8(d). This  $dI/dV$  profile  $f(x)$  is well described with the standard  $180^\circ$ -domain wall profile [29]

$$f(x) = \alpha \left\{ \tanh \left( \frac{x-c}{w} \right) \right\} + \beta, \quad (3)$$

where  $2w$  corresponds to the domain wall width and  $\alpha$  and  $\beta$  are related to spin-dependent and spin-independent  $dI/dV$  signal, respectively [12]. The best fitted parameters of  $2w = 12.9 \pm 2.8$  nm,  $\alpha = 0.042 \pm 0.003$ , and  $\beta = 0.978 \pm 0.002$  were derived from Fig. 8(d). From this measurement, the observed domain wall width is estimated as  $12.9 \pm 2.8$  nm, which is also comparable to that observed on the bulk Cr(001) surface [12] near the screw dislocation.

The feature of the type B spin frustration, however, may be caused by the odd number of adjacent screw dislocations. If the number of adjacent screw dislocations is an odd number of 3, for example, the cancellation of the spin frustration is not easily achieved and more complicated spin frustration may occur. A similar geometrical spin frustration appears in the case of nearest-neighbor AF coupling on a triangular lattice in the two-dimensional system. This geometrical spin frustration can induce a complex magnetic order, such as a Néel ordered state [30]. Using SP-STM combined with first-principles calculations,  $120^\circ$  Néel ground state was observed on single monolayer Cr on the Pd(111) surface [31]. However, lateral scale and magnetic coupling in the present study seems to be much different from the case of AF coupling on a triangular lattice.

Another origin may be the AF domains with different quantization axes, which were reported in our previous study on 4-nm-thick Cr(001) films [15]. Two equivalent domains of surface AF order are allowed due to fourfold symmetry on the Cr(001) surface, where the quantization axes are rotated by  $90^\circ$  with respect to each other. If the quantization axis of the surface AF order were perpendicular to the horizontal quantization axis of the Fe spin moment on the tip, magnetic contrast would not be observed. In our opinion, however, weak magnetic contrast was observed in the spin-frustrated area, which was different from the AF domains with different quantization axes. Therefore, the AF domains with different quantization axes are unsatisfactory for explaining the origin of the spin-frustrated area.

## B. Micromagnetic simulations for spin frustrations caused by two and odd number of screw dislocations

In the following we focus on the consequences of micromagnetic simulation [32] for both types of spin frustration caused by screw dislocations, which modify topological AF ordering on Cr(001) surface. Ravlić *et al.* [12] reported

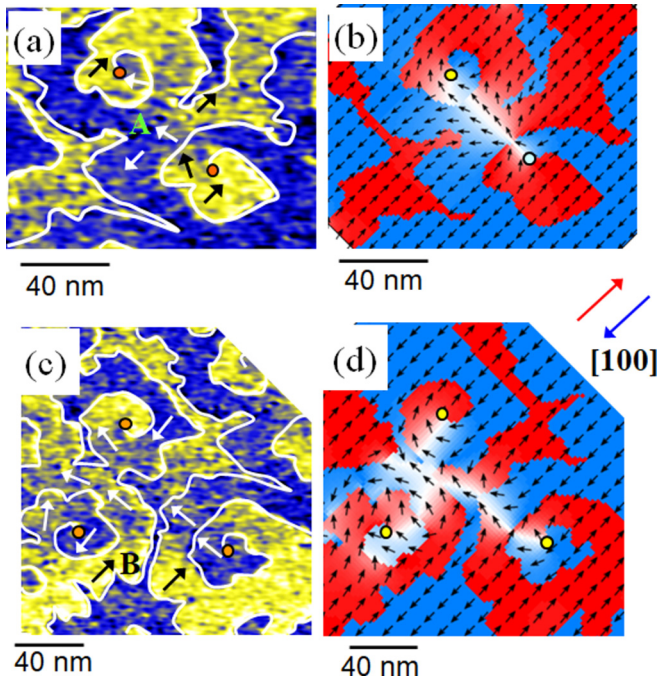


FIG. 9. The experimentally derived  $dI/dV$  magnetic images around region A (a) ( $140 \times 110 \text{ nm}^2$ ) and region B (c) ( $170 \times 180 \text{ nm}^2$ ), where different types of spin frustrations are observed. The directions of the magnetization are represented by the black and white arrows in (a) and (c). Steps and screw dislocations are represented by white lines and orange dots, respectively in (a) and (c). The calculated magnetic structures of (b) and (d) correspond to (a) and (c), respectively. In (b) and (d) the red (blue) contrasts and arrows indicate the parallel (antiparallel) magnetization relative to the  $[100]$  direction, respectively. Screw dislocations are represented by yellow or light blue dots in (b) and (d). The white regions in (b) and (d) correspond to the spin frustration region.

micromagnetic simulation of the spin structure around one screw dislocation in Cr(001), in which the width and the shape of the spin frustration around the dislocation are determined. In our previous study, spin frustration and asymmetric magnetic ordering due to dense spiral terraces were well explained by micromagnetic simulation, in which the spin structure of adjacent two spirals including two screw dislocations was assumed [16]. Therefore, micromagnetic simulation is one of the powerful methods to understand the spin frustration caused by screw dislocations.

In order to directly compare the observed and calculated magnetic structures, slightly magnified magnetic images of around both types of spin frustration are shown in Fig. 9(a) for type A and Fig. 9(c) for type B, respectively. The observed magnetic structures in Figs. 9(a) and 9(c) are deduced from the observed  $dI/dV$  magnetic signal intensity by assuming the orientation of the tip magnetization to be parallel to the bcc  $[100]$  direction and constant magnitude of the Cr magnetic moments. The derived magnetic structure is shown by arrows in which the  $dI/dV$  signals are averaged over several pixels. In Fig. 9(a) the topological AF order and the  $180^\circ$  type domain wall between the two dislocations are clearly identified. On the other hand, complicated magnetic structure appears in the spin-frustrated area (type B spin frustration) in Fig. 9(c).

Higher resolution  $dI/dV$  magnetic imaging may be important for a further understanding of the mechanism of the spin frustration, but is out of the present discussion due to the RT measurement of our STM operation system.

In order to understand the difference of both types of spin frustration on magnetic structures, we examine the magnetic structure through micromagnetic simulations. As the lateral size of the terrace-and-step structure lies in the submicron meter range, the continuum micromagnetic theory was used for calculation. The shape and lateral size of the terrace-and-step structure of the simulation models for both types of spin frustrations are assumed to be almost the same as the STM images.

Since there is no magnetostatic energy owing to the absence of the stray field in AF materials [29], it is not necessary to take into account the demagnetization term in the topological AF structure of the Cr(001) surface [12,16]. Spin frustrations are expected between two dislocations for type A and in the triangular area consisting of three of screw dislocations for type B. Therefore, we have considered the negative (AF) exchange interaction at the step edge and the positive exchange interaction in the single atomic terraces, corresponding to the topological AF order on the Cr(001) surface [12,16]. These interactions and the absence of the demagnetization term are essential for the spin frustration on the topological AF structure of the Cr(001) surface.

In the calculation, a cubic magnetocrystalline anisotropy may be expected due to a fourfold symmetry on the Cr(001) surface. However, the uniaxial effective anisotropy was taken into account in previous micromagnetic simulations [12,16], consistent with the observed  $180^\circ$  domain walls between two screw dislocations in addition to speculated magnetostrictive self-energy [29]. Therefore, in this simulation, we calculated two cases either with the cubic magnetocrystalline anisotropy or the uniaxial effective anisotropy. However, only little difference is recognized in the two cases.

Two equivalent domains of surface AF order are allowed due to fourfold symmetry on the Cr(001) surface. The observed characteristic length scale of AF domain of bulk Cr, however, ranges from tens to hundreds of  $\mu\text{m}$  [33]. Although there is a possibility of difference of the AF domain size between the bulk Cr and thin Cr film surface, it seems to be plausible that a single AF domain with the uniaxial quantization axis is usually observed in the case of the STM image in less than a  $1 \mu\text{m}$  scan area. Therefore, the uniaxial effective anisotropy may be more plausible on the Cr(001) surface, being consistent with the previous results of Cr(001) surfaces [10,14].

The equilibrium magnetic configuration is derived by minimizing the total energy as a function of the orientation of the magnetization under the constraint of constant magnetization. We used the following material parameters for Cr: Exchange stiffness (in the single atomic terrace)  $A_{\text{ex}} = 1 \times 10^{-11} \text{ J/m}$ , the effective uniaxial anisotropy  $K_u = 1.77 \times 10^3 \text{ J/m}^3$ , and the AF exchange interaction at the step edge  $\delta = -2 \times 10^{-3} \text{ J/m}^2$ . These values are the same as those used in the previous study [16]. The uniaxial anisotropy direction is parallel to the  $[100]$  direction. The intrinsic domain wall width (2 $\lambda$ ) calculated by Eq. (2) corresponds to 150 nm. The simulations were performed using the micromagnetic simulation

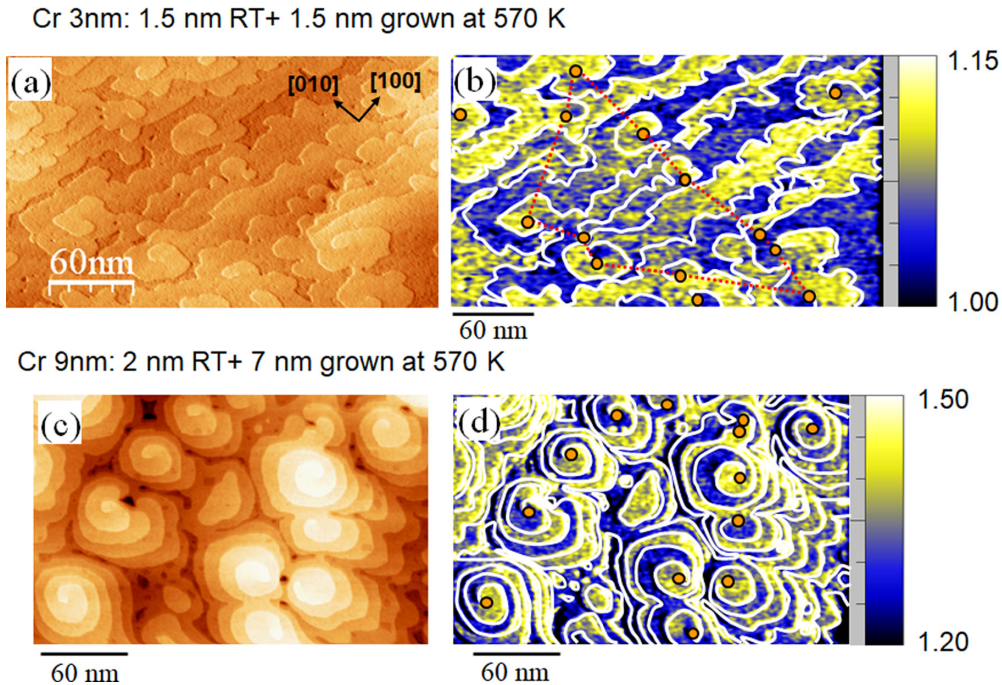


FIG. 10. STM images of the topography (a) and (c), and magnetic  $dI/dV$  map (b) and (d) obtained simultaneously from the same area of Cr(001) film surfaces prepared by using the two-step growth method: (a) and (b) are for the  $d_{\text{Cr}} = 3$  nm film ( $300 \times 175$  nm<sup>2</sup>,  $V_s = -0.2$  V,  $I_t = 0.2$  nA), (c) and (d) are for the  $d_{\text{Cr}} = 9$  nm film ( $275 \times 175$  nm<sup>2</sup>,  $V_s = -0.1$  V,  $I_t = 0.1$  nA). Steps and screw dislocations are indicated in (b) and (d) for clarity purposes by the white lines and orange dots, respectively. Spin-frustrated area in (b) is indicated by red broken lines.

program OOMMF [34]. The mesh cell size of the simulation models are  $0.32 \times 0.32 \times 2$  nm<sup>3</sup> for type A [Fig. 9(b)], and  $0.4 \times 0.4 \times 2$  nm<sup>3</sup> for type B spin frustrations [Fig. 9(d)].

The results of the simulation are presented in Figs. 9(b) and 9(d). The red (blue) and white contrasts indicate that the magnetization is parallel (antiparallel) and in-plane perpendicular to the [100] direction, respectively. While the topological AF order appears in a series of adjacent terraces in both results of the simulations, there is a clear difference of the frustrated region [white regions in Figs. 9(b) and 9(d)] between the two calculations.

In Fig. 9(b) the frustrated region is limited mostly in the straight line between the two screw dislocations, which is the feature of the type A spin frustration. In the vicinity of the upper screw dislocation [indicated by yellow dot in Fig. 9(b)], however, the frustrated region is slightly deviated from the straight line. This is the effect of the individual spiral terrace, as observed in our previous study [14].

In the case of the type B spin frustration shown in Fig. 9(d), however, the frustrated (white) regions are slightly spread out of the triangular region with three corners at the three screw dislocations. These spin frustrations form the complicated magnetic structure, which are nearly consistent with the observed magnetic structure in Fig. 9(c).

### C. Odd spin frustration caused by a cluster of multiple (>10) screw dislocations

Here we additionally report a novel type large scale of spin frustration consisting of a cluster of 11 screw dislocations connected by the red dashed lines in Fig. 10(b) observed for the  $d_{\text{Cr}} = 3$  nm Cr(001) film prepared by the two-step

growth method. Figures 10(a) and 10(b) show the topography and magnetic images ( $300 \times 175$  nm<sup>2</sup>, with  $V_s = -200$  mV) on the same sample surface as Figs. 8(a) and 8(b). But the regions of measurements are different between Figs. 10(a) and 10(b) and Figs. 8(a) and 8(b). We identified 14 screw dislocations in the scanned area of Fig. 10(a). The density of the screw dislocations is significantly higher by a factor of  $10^2$  compared to that of the bulk Cr(001) surfaces [11,12], but approximately 60% compared to that obtained in our previous study on 4-nm-thick Cr(001) films [15]. In the present case in Fig. 10(b), the spin frustration is caused by multiple number of screw dislocations, where the interaction between screw dislocations seems to be very complicated.

In order to understand the origin of the large scale spin frustration as in Fig. 10(b), we show the magnetic structures of 9-nm-thick Cr(001) film prepared by a slightly modified two-step growth (2 nm RT followed by 7 nm 570 K growth) [16], where the surface roughness induced by the individual screw dislocations is noticeably increased. Figures 10(c) and 10(d) display the topographic and corresponding magnetic images of the 9-nm-thick Cr(001) film with the comparable density of screw dislocation as in Fig. 10(a). We find that the spin frustrated area among screw dislocations are limited up to roughly about 4.5% of the scan area of Fig. 10(d), in strong contrast to the large scale spin frustration surrounded by the red dotted line in 3 nm Cr film in Fig. 10(b).

This is because the high winding number of the screw dislocations in this 9 nm film hinders the proximity of the spin frustration, leading to the robust AF order inside each screw dislocation. These results indicate the importance of the delicate balance between the density and winding number of the screw dislocation (nanoscale spiral terraces) on the

emergence of the large-scale spin frustration observed in 3 nm film.

Note that the observed large-scale spin frustration consisting of several screw dislocations was neither observed on the bulk Cr(001) surface [11,12] nor in our previous study on 4-nm-thick Cr(001) films [15].

## V. CONCLUSION

We used STM/STS, LEED, and AES to study the growth and morphology of Cr films ( $d_{\text{Cr}} \leq 3$  nm) on Au(001). It is found that (I)  $d_{\text{Cr}} = 3$  nm: Two-step growth method at RT and 570 K is the optimized growth condition of the Cr(001) thin films. We performed magnetic imaging of these using spin-polarized STS. The observed magnetic image revealed three characteristic features: (1) topological AF order in a series of adjacent terraces, (2) narrow domain walls between the

two screw dislocations, and (3) existence of a spin-frustrated area consisting of a cluster of odd or multiple numbers of screw dislocations. The effects of a cluster with odd numbers of screw dislocations on magnetic structures were demonstrated well through micromagnetic simulations, considering the absence of the demagnetization term, the AF exchange interaction at the step edge, a positive exchange interaction in the single atomic terrace, and the effective anisotropy energy terms.

The AF film surfaces play an important role in pinning ferromagnetic films via the exchange bias effect in spin-electronic devices. Therefore, imaging of both the topological and magnetic structures of AF films is highly desirable, not only for the further development of spin-electronics devices, but also for providing new insights into the underlying physics.

- 
- [1] H. Zabel, *J. Phys.: Condens. Matter* **11**, 9303 (1999).
- [2] M. N. Baibich, J. M. Broto, A. Fert, F. NguyenVanDau, F. Petroff, P. Etienne, G. Creuzet, A. Friederich, and J. Chazelas, *Phys. Rev. Lett.* **61**, 2472 (1988).
- [3] H. Hopster and H. P. Oepen (Eds.), *Magnetic Microscopy of Nanostructures* (Springer, Berlin, 2004).
- [4] M. Bode, *Rep. Prog. Phys.* **66**, 523 (2003).
- [5] S. Heize, M. Bode, A. Kubetzka, O. Pietzsch, X. Nie, S. Blügel, and R. Wiesendanger, *Science* **288**, 1805 (2000).
- [6] M. Hervé, B. Dupé, R. Lopes, M. Böttcher, M. D. Martins, T. Balashov, L. Gerhard, J. Sinova, and W. Wulfhekel, *Nat. Commun.* **9**, 1015 (2018).
- [7] S. Meyer, M. Perini, S. von Malottki, A. Kubetzka, R. Wiesendanger, K. von Bergmann, and S. Heinze, *Nat. Commun.* **10**, 3823 (2019).
- [8] S. Nadj-Perge, I. K. Drozdov, J. Li, H. Chen, S. Jeon, J. Seo, A. H. MacDonald, B. A. Bernevig, and A. Yazdani, *Science* **346**, 602 (2014).
- [9] A. Palacio-Morales, E. Mascot, S. Cocklin, H. Kim, S. Rachel, D. K. Morr, and R. Wiesendanger, *Sci. Adv.* **5**, eaav6600 (2019).
- [10] S. Blügel, D. Pescia, and P. H. Dederichs, *Phys. Rev. B* **39**, 1392 (1989).
- [11] M. Kleiber, M. Bode, R. Ravlić, and R. Wiesendanger, *Phys. Rev. Lett.* **85**, 4606 (2000).
- [12] R. Ravlić, M. Bode, A. Kubetzka, and R. Wiesendanger, *Phys. Rev. B* **67**, 174411 (2003).
- [13] T. Hänke, S. Krause, L. Berbil-Bautista, M. Bode, R. Wiesendanger, V. Wagner, D. Lott, and A. Schreyer, *Phys. Rev. B* **71**, 184407 (2005).
- [14] P. J. Hsu, T. Mauerer, W. Wu, and M. Bode, *Phys. Rev. B* **87**, 115437 (2013).
- [15] T. Kawagoe, Y. Iguchi, A. Yamasaki, Y. Suzuki, K. Koike, and S. Suga, *Phys. Rev. B* **71**, 014427 (2005).
- [16] T. Kawagoe, Y. Iguchi, T. Miyamachi, A. Yamasaki, and S. Suga, *Phys. Rev. Lett.* **95**, 207205 (2005).
- [17] U. Schlickum, N. Janke-Gilman, W. Wulfhekel, and J. Kirschner, *Phys. Rev. Lett.* **92**, 107203 (2004).
- [18] M. Bode, E. Y. Vedmedenko, K. von Bergmann, A. Kubetzka, P. Ferriani, S. Heize, and R. Wiesendanger, *Nat. Mater.* **5**, 477 (2006).
- [19] T. K. Yamada, E. Martinez, A. Vega, R. Robles, D. Stoeffler, A. L. Vazquez de Parga, T. Mizoguchi and H. van Kempen, *Nanotechnology* **18**, 235702 (2007).
- [20] H. Oka and K. Sueoka, *J. Appl. Phys.* **99**, 08D302 (2006).
- [21] J. P. Corbett and A. R. Smith, *J. Magn. Magn. Mater.* **465**, 626 (2018).
- [22] Y.-F. Liew and G.-C. Wang, *Surf. Sci.* **227**, 190 (1990).
- [23] J. de la Figuera, M. A. González, R. Garcia-Martínez, J. M. Rojo, O. S. Hernán, A. L. Vázquez de Parga, and R. Miranda, *Phys. Rev. B* **58**, 1169 (1998).
- [24] D. E. Bürgler, C. M. Schmidt, D. M. Schaller, F. Meisinger, R. Hofer, and H.-J. Güntherodt, *Phys. Rev. B* **56**, 4149 (1997).
- [25] T. Kawagoe, T. Miyamachi, M. Someta, T. Kudo, and S. Suga, *Surf. Sci.* **602**, L15 (2008).
- [26] T. Kawagoe, T. Miyamachi, and S. Suga, *Jpn. J. Appl. Phys.* **51**, 025602 (2012).
- [27] J. A. Stroscio, D. T. Pierce, A. Davies, R. J. Celotta, and M. Weinert, *Phys. Rev. Lett.* **75**, 2960 (1995).
- [28] T. Kawagoe, E. Tamura, Y. Suzuki, and K. Koike, *Phys. Rev. B* **65**, 024406 (2002).
- [29] A. Hubert and R. Schäfer, *Magnetic Domains* (Springer, Berlin, 1998).
- [30] B. Hardrat, A. Al-Zubi, P. Ferriani, S. Blügel, G. Bihlmayer, and S. Heinze, *Phys. Rev. B* **79**, 094411 (2009).
- [31] M. Waśniowska, S. Schröder, P. Ferriani, and S. Heinze, *Phys. Rev. B* **82**, 012402 (2010).
- [32] J. Leliaert and J. Mulkers, *J. Appl. Phys.* **125**, 180901 (2019).
- [33] P. Evens, E. Isaacs, G. Aepli, Z. Cai, and B. Lai, *Science* **295**, 1042 (2002).
- [34] The Object Oriented Micromagnetic Framework (OOMMF) project at NIST (<http://math.nist.gov/oommf/>); We used the OOMMF program, Version 1.2a3.